Equalizing Octagonal PEC Columns with Steel Columns: Experimental and Theoretical Study

Mehdi Ebadi Jamkhaneh, S.M.ASCE[1]; and Mohammad Ali Kafi, Ph.D.[2]

Abstract: Today, the use of composite sections of concrete and steel is increasing. In this study, the behavior of two partially encased composite (PEC) columns is studied experimentally under pure compressive and bending loads. Then a simple analytical method is suggested for PEC columns by introducing all-steel columns, which are composed of four stiffener plates on the four flanges of the steel section. The sizes of the stiffener plates are found by equalizing the compressing strength as well as bending stiffness of the two sections. The accuracy and efficiency of the suggested method was assessed using the FEM in a software program by calculating and comparing the internal forces resulting from analyzing an irregular building. The results indicated high accuracy of the suggested linear static analysis method and meet the need to use finite-element simulations for the users and designers. **DOI: 10.1061/(ASCE)SC.1943-5576.0000375.** *© 2018 American Society of Civil Engineers.*

Author keywords: Partially encased composite (PEC) column; Equivalence steel cross section; FEM; Irregular building.

Introduction

Steel-concrete structures improve the seismic performance of structures and the stiffness of high-rise buildings. The benefit of composite sections is very important in construction and the tall building industry (Oyawa et al. 2016). Additionally, using two material properties leads to an increase in energy absorption (Ebadi Jamkhaneh and Kafi 2017). The partially encased composite (PEC) column is one of the recent achievements in the field of composite columns. Usually, PEC columns are made of three plates filling the gap between the flange and web using concrete. In the common samples in European countries and Canada, web and flange thicknesses are considered equal. Meanwhile, to prevent local buckling strength of the flange from increasing, transverse links are welded to the flange tip between the flanges on equal intervals. In Europe, hot-rolled compressed standard sections are used, which are inherently resistant against local buckling. The concrete cast between the flanges both provides the column axial compressing strength and prevents the column web from local buckling. Moreover, flange deformation toward the column internal part is prevented. On the other hand, transverse links prevent the flange deformation outwardly. Therefore, using these types of composite columns is widely beneficial.

Regarding the PEC columns, several scholars have studied their behavior under axial, bending, and shear loading in experimental and numerical methods. Chicoine et al. (2002a) suggested a numerical model to study the concrete confinement effect, residual stresses, and imperfections in the flanges on total column behavior. Furthermore, in another study (Chicoine et al. 2002b), they assessed the parameters affecting the behavior of such columns, link spacing, flange stiffness, and longitudinal and transverse reinforcements. Begum et al. (2007) modeled finite-element PEC columns under different loading conditions using the dynamic explicit solution strategy. Thin-walled PEC columns filled with high-strength concrete behavior were studied by Begum et al. (2013). The results indicated brittle failure of these columns compared with using concrete of normal strength. Begum et al. (2015) conducted a parametric study on eccentrically loaded PEC columns under major axis bending. Chen et al. (2010) conducted a series of experimental and numerical tests on PEC columns under axial and cyclic loading. They concluded that the transverse link spacing is effective to prevent column flange local buckling with a high width to thickness ratio. Zhao and Feng (2012) investigated the axial ultimate capacity of PEC columns. Their results showed that a closer link spacing improves the ductility of the columns; however, the measurements show that generally yielding does not occur before the peak load in the links. In experimental research Dastfan and Driver (2016) used the PEC columns in a steel shear wall system. The test results indicated that detailing of the PEC columns played an important role in improving the seismic performance of the system. Pereira et al. (2016) studied PEC column behavior under pure axial loading under the presence of longitudinal and transverse steel bars. They demonstrated that the effects of bar presence on load-bearing capacity, stiffness, and postpeak behavior are not significant. Song et al. (2016) investigated the local and postlocal buckling behavior of welded steel shapes in PEC columns. Based on their parametric study, a series of expressions was developed for predicting critical strength and post-buckling strength in PEC columns under concentric loading.

Studies were conducted on the PEC columns and steel column equalization. Marinopoulou et al. (2007) suggested formulas for stimulating the full-steel cross section with the PEC cross section. Begum and Ghosh (2014) conducted numerical simulations of the PEC columns with equivalent steel sections. The simulations of the composite columns with equivalent steel sections are found to predict the experimental behavior of the PEC columns with very good accuracy, whereas simulating the composite members faces several difficulties due to the difficulty of modeling two different materials and their interactions as well as considering shear studs. Therefore, some structural analysis software cannot correctly simulate such composite members, and there are a few types of finite-element software, such as *Abaqus 6.14.2*, *ANSYS 18.2*, and so forth, that are

[1]Ph.D. Candidate, Faculty of Civil Engineering, Semnan Univ., Semnan 19111-35131, Iran. E-mail: mehdi.ebadi@semnan.ac.ir

[2]Associate Professor, Faculty of Civil Engineering, Semnan Univ., Semnan 19111-35131, Iran (corresponding author). E-mail: mkafi@semnan.ac.ir

Note. This manuscript was submitted on October 5, 2017; approved on December 14, 2017; published online on April 13, 2018. Discussion period open until September 13, 2018; separate discussions must be submitted for individual papers. This paper is part of the ***Practice Periodical on Structural Design and Construction***, © ASCE, ISSN 1084-0680.

able to simulate such complex capabilities. However, these are quite expensive and time-consuming and using them presents difficulties.

As the first objective of this paper, behavior of some PEC specimens with an octagonal cross section under compressive and bending loads is experimentally studied. Then, an appropriate linear elastic analysis for an equivalent full-steel cross section of columns is suggested. There are two key factors in stimulating these two cross sections: the compressive strength and the bending stiffness. For simplification purpose, sizes of the plates added to the original steel cross section will be logical and comparable to the latter. Eventually, verification performed using the PEC column tests and the relevant results were compared. Finally, a comparison was conducted between the column internal forces of a 2-story steel structure and the PEC column structure under gravity and lateral loads using FEM.

Test Description

Two groups of one-third-scale PEC columns with dimension of $0.15 \times 0.15 \times 1$ m were constructed. Fig. 1 shows typical PEC column geometric parameters. Parameters illustrated in the concrete-side elevation view [Fig. 1(a)] are the column length, L, and the center-to-center spacing of the links, s. Parameters illustrated in the plan view [Fig. 1(b)] are the column depth, d, the overall flange width, b_f, the flange thickness, t_f, and the web thickness, t_w. The steel section was fabricated from st37 grade. The nominal plate thickness of the flange and web were 6 and 3 mm, respectively. The nominal flange width to thickness ratio for the columns was 10. This value is lower than the maximum flange width to thickness ratio of 32 specified by CSA S16-14 (CSA 2014). The columns have a constant link spacing equal to 100 mm, and all of the links have a diameter of 6 mm. The transverse links are set back from the flange tips so that there is 10 mm of clear concrete cover between the link and the concrete face, regardless of the link diameter. Columns were cast with normal-strength (nominally 25 MPa) concrete in the test region. A summary of the PEC column characteristics is listed in Table 1. The end zones of the columns (0.05 m of column length at each end) were strengthened by stiffeners to prevent possible failure at these locations due to uneven loading.

Concrete Mix Design and Properties

The main properties of interest during the mix design were strength and workability. The mix design is presented in Table 2. The concrete was made with locally available materials, and 12.5-mm crush coarse aggregate was used. The fine aggregate had a fineness module of 2.4. Considering that the typical concrete density of the mix was 2,300 kg/m^3, the elastic modulus of the normal-strength concrete (23.715 GPa) is within typical range of American Concrete Institute (ACI) *Manual of concrete practice* report ACI-318-08 (ACI 2008). The average strain at peak stress of the normal-strength concrete is 2,225 $\mu\varepsilon$, which is a typical value. The Poisson's ratio of the normal-strength concrete (0.13) is typical of accepted values (0.11 to 0.21) for normal-strength concrete according to ACI report 363R-92 (ACI 1997). The typical stress-strain curve for the normal-strength concrete obtained from this study is illustrated in Fig. 2.

Steel Plate and Rod Properties

All coupon tests were conducted in an MTS 1000 universal testing machine (MTS Systems, Eden Prairie, Minnesota) with a tensile capacity of 1,000 kN, at the Structural Engineering Laboratory of Semnan University, Semnan, Iran. Load measurements were taken

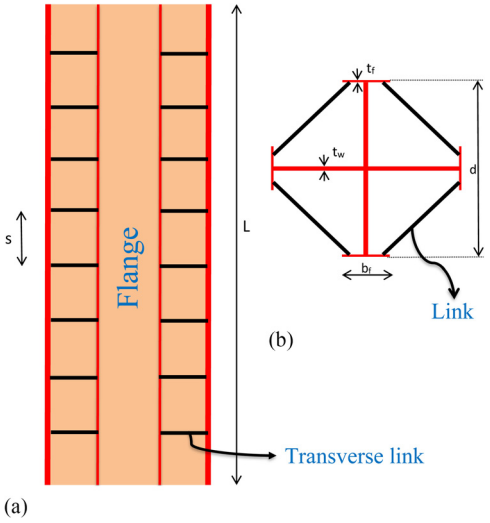

Fig. 1. Geometry of a PEC column on the (a) steel-side elevation and on the (b) plan view

Table 1. Characteristics of Test Specimens

Characteristic	PEC-1	PEC-2
Section dimension $b_f \times d$ (mm)	60 × 150	60 × 150
Length [L (mm)]	1,000	1,000
Thickness of flange, web (mm)	6.3	6.3
Flange width to thickness (b_f/t_f)	10	10
Link	—	—
Spacing (mm)	100	100
Diameter (mm)	6	6
Longitudinal bar	—	—
Number	0	4
Diameter (mm)	0	16

Table 2. Concrete Mix Design at Saturated Surface Dry Conditions

Material	Weight (kg)
Water (W)	215
Cement (C)	430
Coarse aggregate	1,053
Fine aggregate	617

using the internal load cell of the MTS 1000. The stress versus strain curves generated are typical of hot-rolled structural grade steels. The results of the steel plate tension coupon tests can be found in Table 3. All links of a particular diameter were cut from rods of the same heat of steel, as were additional pieces acquired for material testing. Four tension coupons were tested from the steel rods. Two of the coupons were cut from the 6-mm steel rod used as links. The other two were cut from the 14-mm steel rod used as longitudinal rebar. The coupons were tested according to ASTM Standard A370 (ASTM 2003) shown in Table 3 (unit in megapascals for stress and microstrain for strain).

Test Setup and Procedures

Both PEC columns were tested at the structural laboratory in Semnan University. Columns were tested with a fixed-end condition on one side and a vertical slide on the other side. The two test

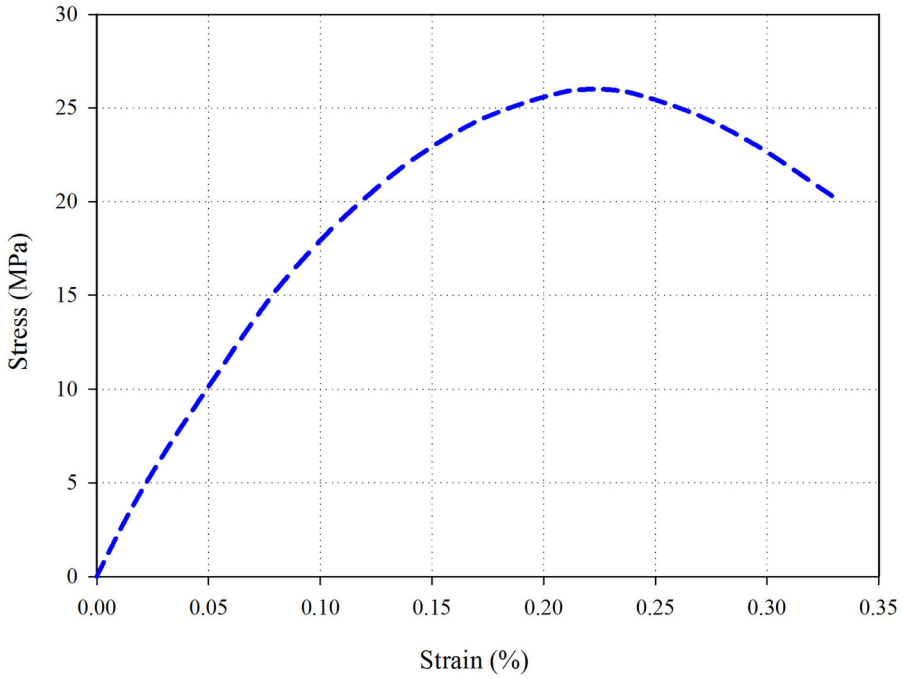

Fig. 2. Typical stress-strain curve for normal-strength concrete

Table 3. Tensile Test Results for Steel Plate and Steel Rod

Element	Yield stress (MPa)	Ultimate stress (MPa)	Yield strain ($\mu\varepsilon$)	Hardening strain ($\mu\varepsilon$)	Rupture strain ($\mu\varepsilon$)
Plate	257	389	1,951	16,900	320,000
Rod	297	412	1,568	23,200	451,000

setups (concentric and eccentric loading conditions) required a different instrumentation, but they used the same testing machine and data acquisition system.

A test of the columns under concentric compressive loading was performed using a testing system machine that has a loading capacity of 2 MN. The load cell applies a compressive force horizontally and has a maximum stroke of 400 mm. The base of the universal testing system (UTS) sits horizontally on a frame.

Concentric Test Loading Protocol

The loading procedure was similar for each of the two tests. The primary force rate (5 kN/min) was used to control the UTS. The test began at a force rate of 50 kN/min until the displacement reached approximately 0.05 mm, during which the electronic data were scrutinized to ensure that all channels were functioning properly. Following this, the force rate was increased to 75 kN/min until the real-time graphs of the column behavior indicated that the column stiffness was decreasing (typically about 80% of the peak load). To minimize dynamic effects, the force rate was then decreased back to 50 kN/min until failure of the column occurred. If the failure resulted in a sudden drop in column capacity, the force of the UTS was held constant until the measured UTS displacement had stabilized and photographs had been taken. Loading was then changed to displacement control at a stroke rate of 0.06 mm/min. If the failure resulted in a gradual drop in capacity, then the stroke rate was held at 0.06 mm/min until the column capacity had been reduced to below 85% of the peak load. Then, the rate was increased to 0.08 mm/min. Regardless of the failure type, once the degradation of postpeak strength began to slow significantly, defining a reasonably stable residual strength plateau, the stroke rate was increased to 0.1 mm/min. The column was then unloaded and the unloading behavior was recorded. Fig. 3 shows the concentric load test setup.

Eccentric Test Loading Protocol

The loading procedure throughout the test was similar to the concentric loading protocol. The only difference in loading with eccentricity compared with the coaxial loading is that two different directed loads are imposed to the rigid beam above the column with respect to the column center (Fig. 4).

Test Results and Discussion

Results of Concentric Specimens under Axial Compressive Loading

A summary of the peak test loads and predicted loads in codes [CSA S16-14 and EN 1994-1-1; CEN (2004)] for the PEC columns that were loaded concentrically is presented in Table 4. The predicted column load was computed using Eqs. (1) and (2)

$$C_{\mathrm{rc}} = \left(\phi A_{\mathrm{se}} F_y + 0.95\alpha_1 \phi_c A_c f_c' + \phi_r A_r F_{\mathrm{yr}}\right)\left(1 + \lambda^{2n}\right)^{1/n} \tag{1}$$

$$N_{\mathrm{pl,Rd}} = A_a f_{\mathrm{yd}} + A_s f_{\mathrm{sd}} + 0.85 A_c f_{\mathrm{cd}} \tag{2}$$

where factored compressive resistance $N_{\mathrm{pl,Rd}} = C_{\mathrm{rc}}$; resistance factor of structural steel $\phi = 0.90$; resistance factor of concrete

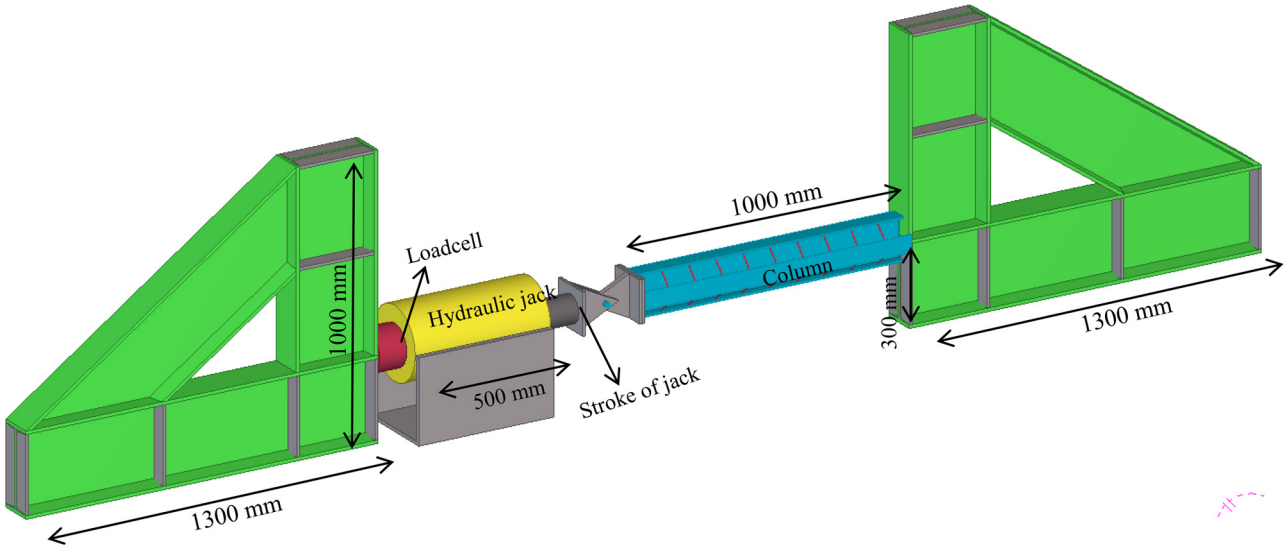

Fig. 3. Setup for concentric compression loading (Units: millimeters)

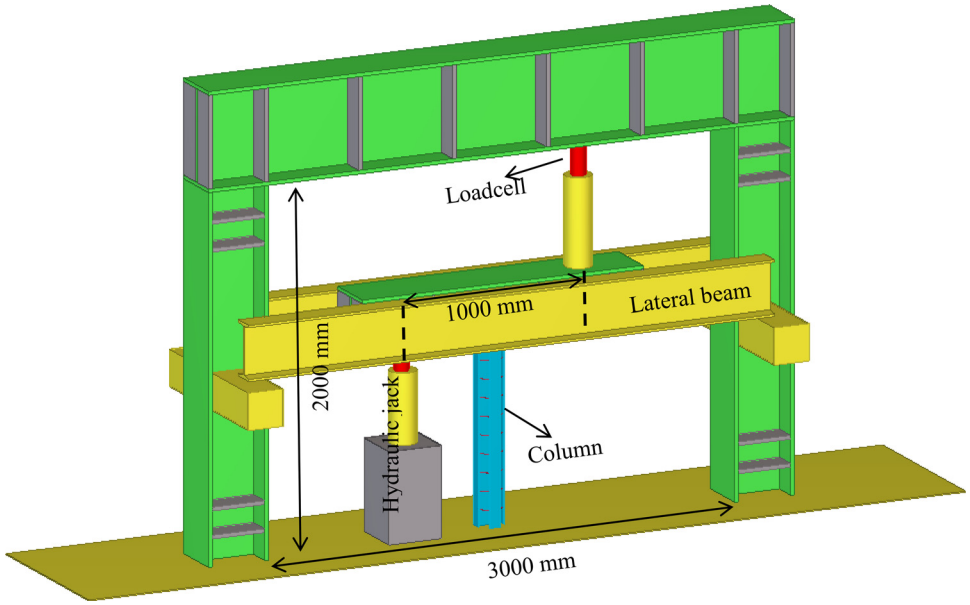

Fig. 4. Setup for pure moment loading

Table 4. Comparison of Peak Test Loads between Experimental and Predicted Results

Specimen	$P_{(Exp)}$ (kN)	$P_{(CSA)}$ (kN)	$P_{(EN)}$ (kN)	$P_{(Exp)}/P_{(CSA)}$	$P_{(Exp)}/P_{(EN)}$
PEC-1	802.5	688.285	875.881	1.166	0.916
PEC-2	1105	895.605	1117.033	1.234	0.989

$\phi_c = 0.65$; resistance factor of reinforcing steel bars $\phi_r = 0.85$; A_{se} = effective steel area of the steel section; A_c = area of concrete; A_r = area of longitudinal reinforcement; $f_{sd} = F_y$ = yield strength of steel plate; $f_{cd} = f'_c$ = compressive strength of concrete; $f_{yd} = F_{yr}$ = yield strength of steel bar; λ = slenderness parameter; $\alpha = 0.85 - 0.0015 f'_c$ (but not less than 0.73); and $n = 1.34$.

$$\lambda = \sqrt{\frac{C_p}{C_{ec}}} \tag{3}$$

$$C_{ec} = \frac{\pi^2 EI_e}{(KL)^2} \tag{4}$$

$$EI_e = EI_s + \frac{0.6E_cI_c}{1 + C_{fs}/C_f} \tag{5}$$

where C_{fs} = sustained axial load on the column; C_f = total axial load on the column; I_s and I_c = moment of inertia of the steel and

concrete areas, respectively, as computed with respect to the center of gravity of the cross section; $C_p = C_{rc}$ computed with ϕ, ϕ_c, and $\phi_r = 1.0$ and $\lambda = 0$; C_{ec} = critical loading; E_c = modulus of elasticity of concrete; E = modulus of elasticity of steel; KL = effective length of column; and I_e = equivalent moment of inertia.

Because the test specimens are stub columns, their slenderness parameter, λ, was set to zero for the calculation of the column capacity. For all test specimens, the test load exceeded the predicted capacity from the CSA S16-14 equation. The column containing steel rebar, PEC-2, has the highest test-to-predicted load corresponding to the CSA S16-14 equation ratios, 1.23.

The Canadian standard conservatively presumed the probability of local buckling of the column section by reducing the cross section of its flange. This assumption reduced the calculated compressive bearing capacity compared with laboratory values because in the case of the laboratory specimen, flange buckling was not observed before the sample rose to its maximum capacity. On the other hand, the equation used by the Eurocode standard (CEN 2004) considered flange buckling as improbable and it only applied the concrete confinement coefficient. Applying simple presuppositions increases the bearing capacity of the laboratory sample. Therefore, in this case one could note that the equation detailed in the CSA S16-14 standard compared with the one introduced in the Eurocode standard (EN 1994-1-1) is conservative and more suitable for designing the parts.

Load-Displacement Relationships

Fig. 5 shows the axial load-displacement responses of the two concentric tested specimens. The values of initial stiffness and maximum load and displacement are presented for each specimen in Table 5. The initial stiffness was derived from a linear regression analysis within the elastic range of the load-displacement response. Considering the chart, the load-bearing capacity of PEC-2 is equal to 1,105 kN, which is roughly 38% higher than the PEC-1 column. This is also due to the existence of four longitudinal bars with a 14-mm diameter. The presence of these bars, in case of the meeting buckling strength, roughly increases 238 kN, whereas the balance of the force (approximately 63 kN) is provided by further concrete encasing. Adding such longitudinal bars has managed to increase the displacement in the maximum load up to 33%, which in turn results in further specimen deformability and increased energy absorption. Also, the PEC-2 sample axial stiffness is roughly 8% bigger than that of PEC-1.

Failure Mode

PEC-2 had a failure mode of concrete crushing combined with local buckling of the steel flanges, whereas Column PEC-1 had a link weld fracture followed by concrete crushing combined with local buckling of the flanges. No local buckling of the flanges was observed for any of the columns before the peak load was reached. Although the failure modes of columns were approximately similar, the point at which the failure (marked by a sudden drop in load-bearing capacity) occurred compared with the peak capacity was different depending on the presence or absence of steel rebar. Columns exhibited sudden failure at their peak load. Typically, the failure region was located between adjacent links [Fig. 6(b)]. By removing the crushed concrete after the test, distinct shear-failure planes were exposed. The depth of the shear planes is related to the link spacing. For the closest link spacing the shear-failure plane was only as deep as the links themselves. This resulted in small amounts of concrete spalling off of the column. However, for the largest link spacing or fracturing of links (200 mm), the shear-failure plane extended to a point closer to the web than the concrete surface. This resulted in large pieces of concrete exploding out of the column as

Table 5. Performance Measures of Load and Displacement Capacities and Initial Stiffness

Specimen	P (kN)	Δ (mm)	K (kN/mm)
PEC-1	802.5	4.02	216.63
PEC-2	1,105	5.37	234.15

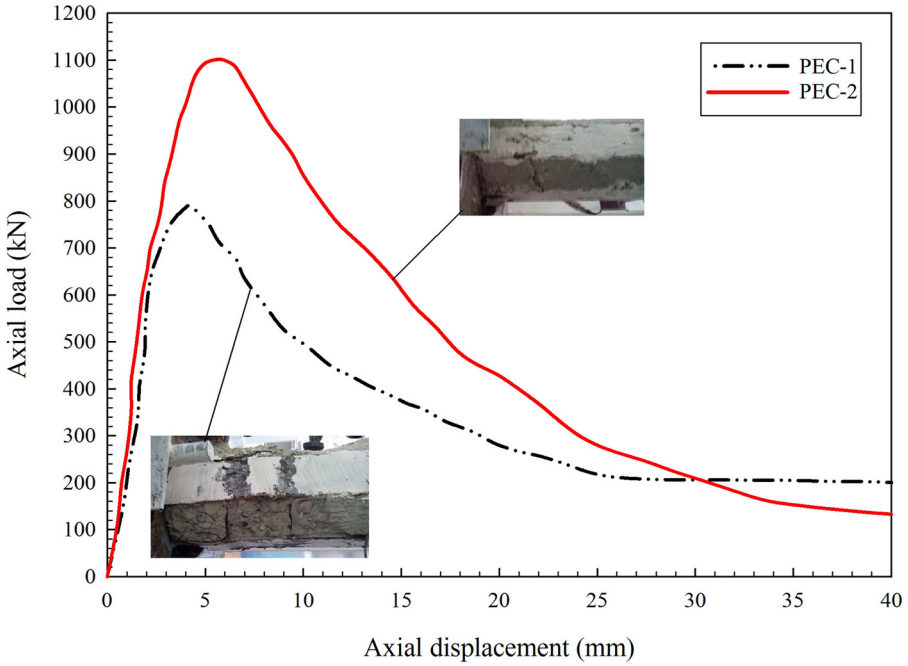

Fig. 5. Axial load-displacement curves of specimens

Pract. Period. Struct. Des. Constr., 2018, 23(3): 04018012

failure took place. The relationship between the shear-plane depth and the link spacing was expected because the closer link spacing provides a higher degree of confinement to the concrete.

Before reaching peak loading in Specimen PEC-1, minor cracking at the end of the column and removal of the priming paint on flange faces occurred. A sudden drop in capacity occurred immediately after reaching the peak load (802.5 kN). At peak load, side flanges buckled and the concrete adjacent to the left side of the column was crushed [Fig. 6(a)]. Two bangs were heard as the link welds fractured when the load reached 600 kN. Throughout the postpeak loading, web plates were buckled at 200 mm at the top of the column. Immediately thereafter the upper flange situated near the end support buckled at 480 kN. Near the end of the test, the weld between the second link at the first 200 mm and the flanges fractured. By fracturing the welds, the unsupported flange length increased, which resulted in the ultimate buckling of the flange; the lengths of this fractured zone were approximately 300 mm, which extended into adjacent zones gradually. During the failure of Specimen PEC-2, cracks were evident at the first 200 mm and light spalling of the concrete was took place at this zone [Fig. 6(b)]. After a sudden drop in capacity, the concrete near the support was crushed and the upper and bottom flanges buckled. During the postpeak loading, a transverse crack propagated along the centerline of the links. The fillet weld between the flange and web plate fractured through the postpeak period. Additionally, at peak load, buckling of longitudinal rebars occurred, which resulted in cracking and spalling of the concrete.

Longitudinal Strain and Transverse Displacement

Longitudinal and transverse strain gauges were installed 350 mm away from the place of force application, namely, on the flange and web of steel section of the column (Fig. 7). Fig. 8 shows the variation of the longitudinal strain of the flange and web against the total longitudinal strain of Column PEC-1. The variation of the strain rate of the web is similar to the total variation rate of the column. Therefore, the longitudinal strain of the web is not affected by the presence of links. However, the variation model for the section flange was different. The flanges start to fail locally before the total strain of the column reaches 2,000 $\mu\varepsilon$. Therefore, the longitudinal stain of the flange is affected by transverse links. This might be due to the residual stresses caused by the welding of the links or to strains caused by concrete shrinkage. Concrete shrinkage reduces the residual stress of the steel insignificantly. However, local stresses of the link are not taken into account for calculation of mean strain. Without consideration of the subject, the premature failure of the flange near the support reduces load-bearing capacity of the column. This is due to the ductility of the steel, which allows retention of the column capacity up to its point of failure. In addition, the presence of links along the entire column avoids premature failure and buckling of column flanges.

Based on Fig. 9, there are two LVDTs on the sides of lateral flanges: one of the displacement meters is compressed and the other shows positive displacement. The displacement Transducer No. 2, which was 200 mm away from location of load application, initially showed positive displacement (i.e., buckling toward the bottom of the floor of the laboratory) but a change of direction occurred after maximum force, development of failure, and buckling at the top of the column.

(a) (b)

Fig. 6. Buckling of flanges, crushing concrete, and fracturing and welds: (a) PEC-1; (b) PEC-2

Transverse Strain Measurements and Transverse Stresses

To highlight the effect of concrete confinement due to steel cross section and concrete expansion, a biaxial stress mode is presumed

$$\begin{bmatrix} \sigma_L \\ \sigma_T \end{bmatrix} = \frac{E}{1-\upsilon^2}\begin{bmatrix} 1 & \upsilon \\ \upsilon & 1 \end{bmatrix}\begin{bmatrix} \varepsilon_L \\ \varepsilon_T \end{bmatrix} \tag{6}$$

where σ_L and σ_T = longitudinal and transverse stresses, respectively; E = measured elastic modulus of the steel plate (200 GPa); ν = Poisson's ratio for steel (0.3); and ε_L and ε_T = longitudinal and transverse strains, respectively, measured by the strain gauges. The von Mises criterion was then used to evaluate the yielding of the biaxial stress state as follows:

$$\sigma_{\text{VM}}^2 = \sigma_L^2 - \sigma_L\sigma_T + \sigma_T^2 \le F_y^2 \tag{7}$$

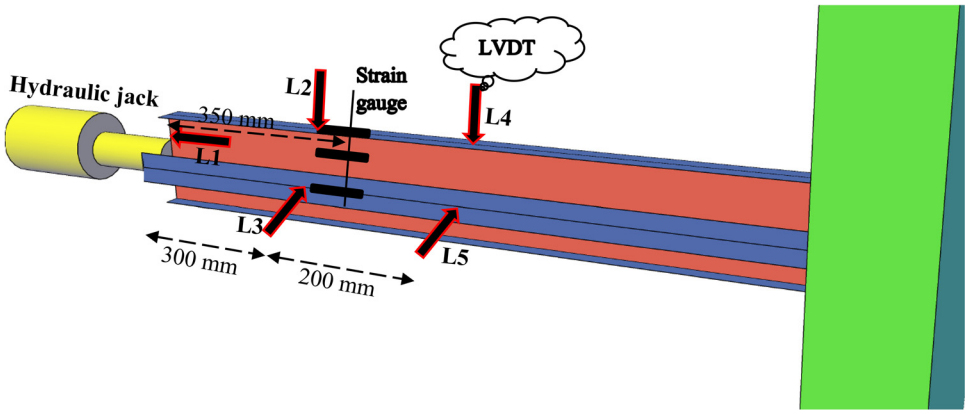

Fig. 7. Location of strain gauges and LVDTs

Pract. Period. Struct. Des. Constr., 2018, 23(3): 04018012

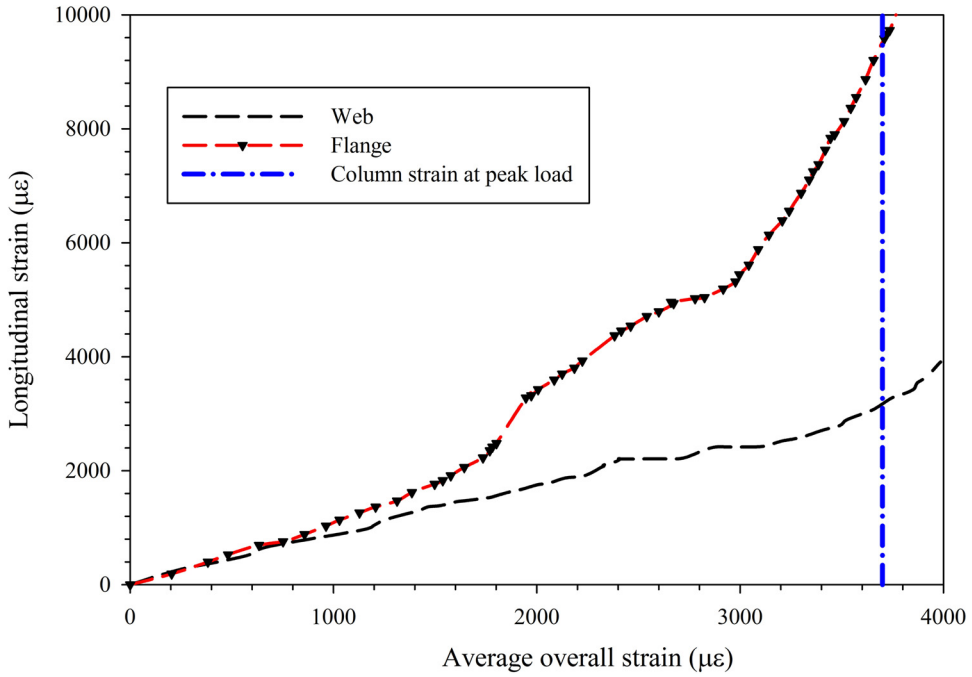

Fig. 8. Typical gauge strains versus average overall strain (Column PEC-1)

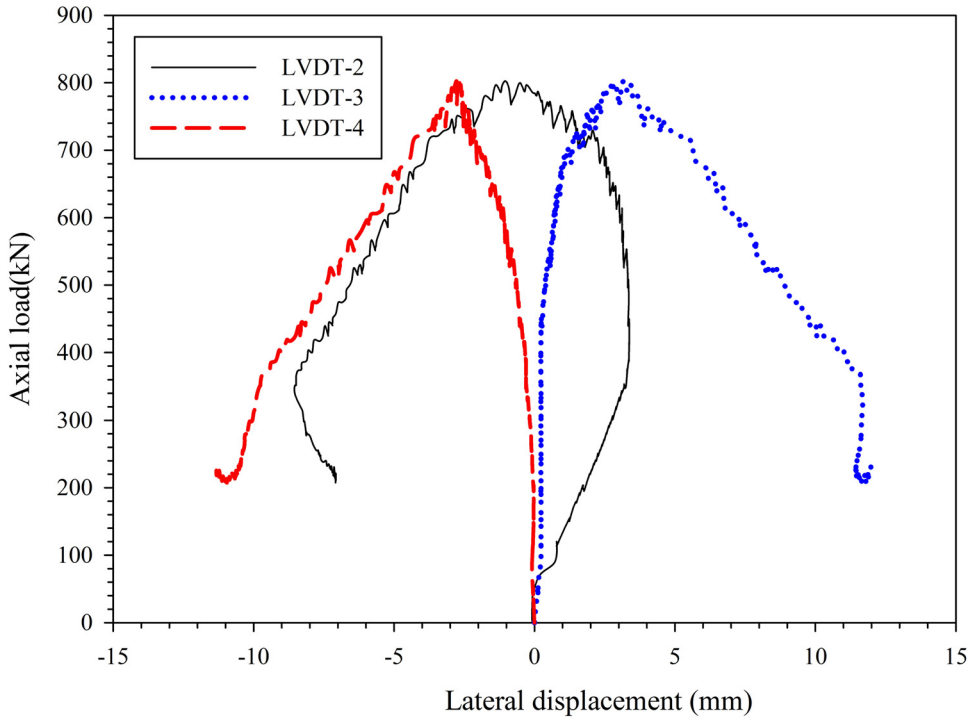

Fig. 9. Axial load-lateral displacement curve (Column PEC-1)

where σ_{VM} = von Mises equivalent stress; and F_y = static uniaxial yield strength of the steel plate (257 MPa). The plate yields when σ_{VM} equals F_y.

Two pairs of strain gauges (each pair includes a longitudinal and transverse strain) were installed on the flange and web of the steel section of the column. A summary of results from measuring the flange and web longitudinal and transverse stresses is presented in Table 6. In this table, σ_L/σ_{VM} is the ratio of longitudinal stress to the von Mises stress when the steel yields. When the von Mises yield criterion was satisfied, σ_L/σ_{VM} was close to 1.0 for each column for both the flange and the web, and σ_T ranged from 16 MPa of compression to 23 MPa of tension. Therefore, transverse stress exerts an insignificant effect on axial load-bearing capacity of the steel section of the flange and web.

Results of Eccentric Specimens under Pure Moment Loading

Moment-Rotation Relationships

Fig. 10 shows the relationship between the column base moment and the head rotation for the two tested columns. Pure moment is created by applying two concentrated loads of different directions at either side of the column 1 m apart from each other. The figure shows that the existence of the concrete portion enhances the moment capacity following a nonlinear trend. The highest initial bending stiffness was also seen in Specimen PEC-2.

By using longitudinal rebars in Column PEC-2, an increase of 4% in moment strength was observed compared with Column PEC-1. However, the enhancement of deformability and rotational capacity is much more evident in the reinforced specimen; the presence of longitudinal rebars increases the compressive strength and rotational capacity of the specimens much more than it increases the moment capacity of them. During the initial linear portion of the moment-rotation diagram, the measured stiffness (slope of the curve) should be close to the theoretical initial stiffness. The theoretical initial stiffness can be calculated by adding the steel section stiffness to the concrete stiffness as follows:

$$(EI)_{\text{PEC}} = EI_S + E_C I_C + E_r I_r \tag{8}$$

where $(EI)_{\text{PEC}}$ = theoretical initial composite column stiffness; E, E_c, and E_r = elastic modulus of the steel plate, concrete, and rebar; and I_s, I_c, and I_r = moment of inertia of the steel, concrete, and rebar section. In determining I_c, the stiffness of the concrete in tension is neglected because cracking in tension takes place at low strains. The theoretical initial stiffnesses for Columns PEC-1 and PEC-2 are 1,450 and 1,452.2 kN · m^2, respectively. The initial predicted column stiffness in CSA S16-14 for all columns is 1,088 kN · m^2. Also, the values that correspond with EN 1994-1-1 are 1018.4 kN · m^2 for PEC-1 and 1,163 kN · m^2 for PEC-2. The initial measured column stiffnesses are 1,108 and 1,127 kN · m^2 for PEC-1 and PEC-2, respectively. These values are less than the theoretical stiffnesses by 23 and 22% for Columns PEC-1 and PEC-2, respectively, because the theoretical values do not consider the geometric imperfections and material variability that are present in the actual columns.

Table 6. Biaxial Stress State of the Steel Plate at Yielding

Specimen	Element	σ_L(MPa)	σ_T(MPa)	σ_{VM}(MPa)	$\sigma_L/\sigma_{\text{VM}}$
PEC-1	Flange	259	11	257	1.008
	Web	253	–23	257	0.984
PEC-2	Flange	261	8	257	1.015
	Web	259	16	257	1.008

Failure Mode

In Column PEC-1, deep cracks were generated in concrete cover at a force level of 45 kN; afterward the cover spalled at the upper section of the column in the vicinity of the beam-column connection. Fig. 11(a) shows that concrete cracking is more evident in the upper parts of the columns and that there is an increase in the removal of paint at the end of the loading. In Column PEC-2, nothing occurred prior to a load level of 37 kN, but soon afterward the removal of color at both compressive and tensile sections of the mid and upper parts of the column took place. Buckling occurred in the vicinity of the beam-column connection at a force level of 42 kN corresponding to an axial displacement of 64 mm. As loading continued, it was seen that welding of the transverse links ruptured at the buckled zone and portions of the concrete spalled [Fig. 11(b)]. Two faces of concrete in compression spalled, and two other faces in tension generated deep cracks. This is the result of larger bracing spans for the concrete (200 mm).

Longitudinal Strain and Transverse Stresses

Longitudinal strain gauges were installed 200 mm away from the location of the application of force on the flange and web of the steel

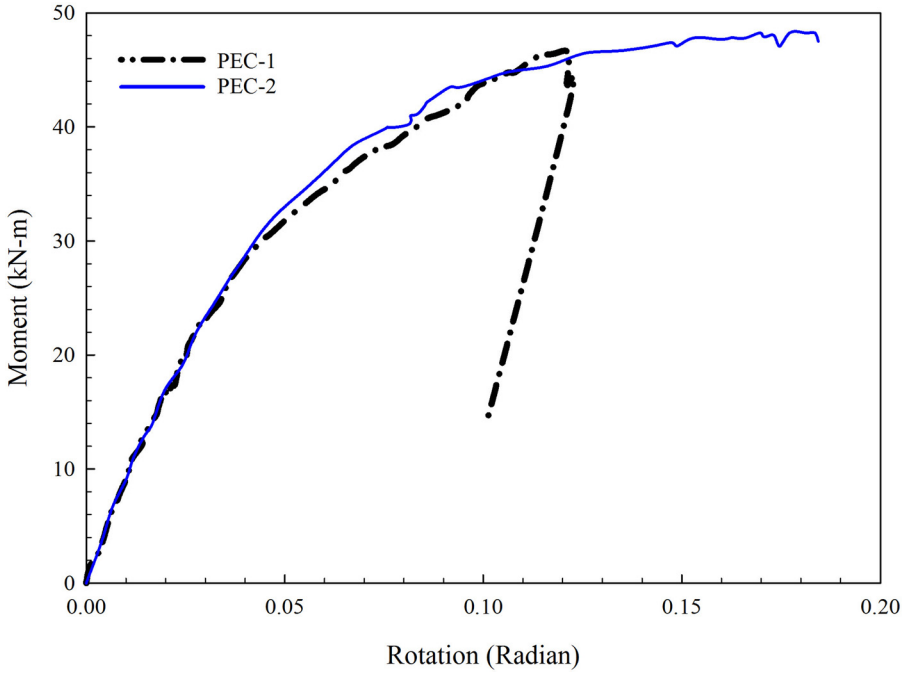

Fig. 10. Moment-rotation curves

section of the column. Fig. 12 shows variation of strain of the flange and web of the two specimens. Evidently, flanges at the tensile zone exceeded failure strain and the web of the steel section did not have failure strain. To analyze the confinement pressure on the steel shape due to the lateral expansion of the concrete, a biaxial stress state was assumed, which was determined using the procedure and residual stress pattern described. A summary of the transverse stresses at yielding (i.e., when the von Mises stress, σ_{VM}, equals the steel yield stress, F_y) for the flange and web is presented in Table 7 for both columns. When the von Mises criterion was reached, σ_L/σ_{VM} was slightly greater than 1.0 for each column, indicating that the transverse stress did not reduce the axial capacity of the steel section. Moreover, despite the fact that the measured transverse strains were tensile as a result of the Poisson effect, the average stress σ_T ranged from 8 to 85 MPa of compression, implying that confinement of the concrete may not have been taking place at these load levels. (However, as mentioned in the previous section, the steel section provided significant confinement to the concrete during the hinge formation when the column was bent about its axis.)

Fig. 11. Failure mode in PEC columns under pure moment loading

Equivalence Steel Cross-Section Formulation

The equivalence or fictitious steel cross section includes a PEC main steel cross section plus certain additions of thin plates on its flange and web. The position of these plates and equivalence full-steel cross section is shown in Fig. 13. The fictitious full-steel and

Table 7. Biaxial Stress State of the Steel Plate at Yielding

Specimen	Element	σ_L(MPa)	σ_T(MPa)	σ_{VM}(MPa)	σ_L/σ_{VM}
PEC-1	Flange	293	85	261	1.122
	Web	243	13	237	1.025
PEC-2	Flange	283	43	264	1.072
	Web	238	8	234	1.017

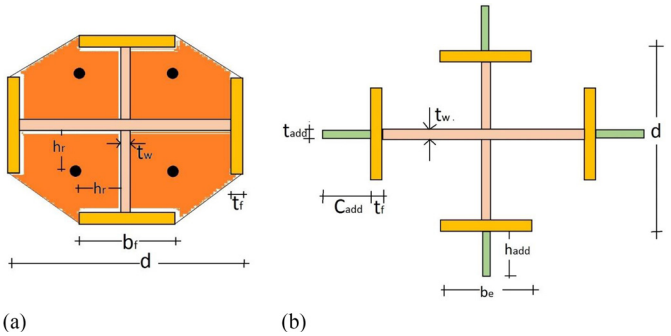

Fig. 13. Simulation of composite steel–concrete cross section: (a) PEC cross section; (b) fictitious steel cross section

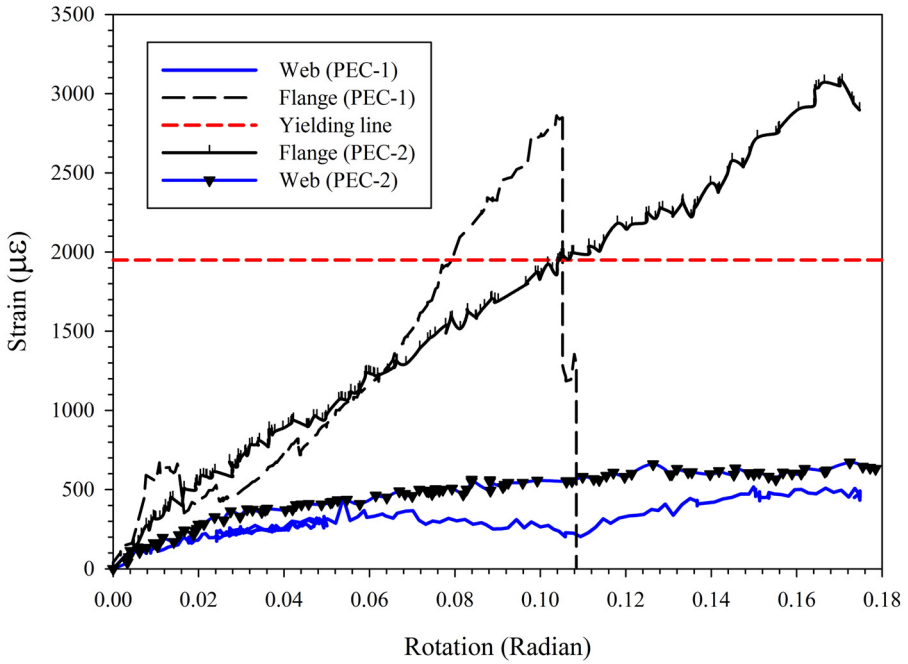

Fig. 12. Strain-rotation curve of the flange and web of the columns

PEC cross sections were considered similar in terms of compressing strength and flexural stiffness. The additional plates on the original steel cross section sizes are found considering the algebraic formulas and through equalizing their compressing strength and flexural stiffness around two axes.

Equivalence in Compressive Strength

PEC compression resistance includes steel cross-sectional plastic strength, steel transverse links, and concrete. The total equivalence steel cross-sectional area is equal to the total initial steel cross sectional area and additional plates on the same

$$P_{\text{plastic}}^{\text{actual}} = A_s f_s + A_c f_c + A_r f_r$$
$$P_{\text{plastic}}^{\text{fictitious}} = (A_s + A_{\text{add}}) f_s \tag{9}$$

According to balance conditions in compressing strength and considering Eq. (9)

$$A_{\text{add}} = A_c \frac{f_c}{f_s} + A_r \frac{f_r}{f_s} = A_c \varphi_c + A_r \varphi_r = A_c(\varphi_c + \rho_r \varphi_r) = A_c \Phi \tag{10}$$

where ρ_r, φ_c, φ_r, and Φ = reinforcement ratio, concrete-to-steel designed stress ratio, bar-to-steel designed stress ratio, and encasing-to-steel designed stress ratio, respectively.

As seen in Fig. 13(a), the total area of the composite cross section is equal to the total areas of cross section of steel (A_s), concrete (A_c), and longitudinal bars (A_r)

$$A_T = 0.5d^2 + db_f - 0.5{b_f}^2$$
$$A_T \equiv A_s + A_c + A_r = A_s + (1 + \rho_r) A_c$$
$$A_c = \frac{A_T - A_s}{1 + \rho_r} \tag{11}$$

Normalization is conducted using the total area (A_T) when determining Eq. (11) and replacing the same in Eq. (10) as per Eq. (12). The result of this formula is a fixed positive value

$$\frac{A_{\text{add}}}{A_T} = \frac{A_c}{A_T}\Phi = \frac{\Phi}{1 + \rho_r}\frac{A_T - A_s}{A_T} = \Phi\frac{1 - \rho_s}{1 + \rho_r} = \frac{\rho_s'}{\rho_r'}\Phi = m^2 \tag{12}$$

On the other hand, the area of the four plates added to the original steel cross section [Fig. 13(b)] may be calculated using Eq. (13)

$$A_{\text{add}} = 2C_{\text{add}}\, t_{\text{add}} + 2h_{\text{add}}\, t_{\text{add}} \tag{13}$$

After Eq. (13) normalization (by dividing the same by A_T), the χ and λ parameters are introduced

$$\frac{A_{\text{add}}}{A_T} = 2\chi + 2\lambda \tag{14}$$

A new formula is generated to calculate the equivalence steel cross-sectional sizes by equalizing the right sides of Eqs. (12) and (14), in which there are geometrical and mechanical specifications of the materials under elastic state

$$2\chi + 2\lambda = m^2 \tag{15}$$

Equalizing in Stiffness

Whereas the relevant cross section has two symmetric axes and the hardness in both directions is the same, only one axis is considered in calculating hardness. Composite and equivalence cross-sectional bending hardness may be calculated using Eq. (16)

$$EI^{\text{actual}} = E_s I_s + E_r I_r + E_c I_c$$
$$EI^{\text{fictitious}} = E_s I_s + E_s I_{\text{add}} \tag{16}$$

Different codes consider the variety of values for concrete stiffness. However, it does not affect the suggested procedure in this article. By applying balance conditions on the stiffness around one of the axes, a parameter, namely, concrete-to-steel elasticity module (Γ_c), is introduced.

$$I_{\text{add}} = I_r + \frac{E_c}{E_s} I_c = I_r + \Gamma_c I_c \tag{17}$$

Considering Fig. 13(a)

$$I_T = I_s + I_c + I_r$$
$$I_s = A_s r^2$$
$$I_r = A_r {h_r}^2 = \rho_r A_c {h_r}^2 \tag{18}$$

The I_T value is calculated using Eq. (19)

$$I_T = \frac{47}{576}d^4 - \frac{{b_f}^4}{576} + \frac{d^2{b_f}^2}{192} + \frac{d^3 b_f}{144} + \frac{d{b_f}^3}{144} - \frac{d^3}{6} - \frac{{b_f}^3}{12} - \frac{5d^2{b_f}^2}{12} + \frac{d{b_f}^2}{3} \tag{19}$$

Eq. (11) may be rewritten as Eq. (20)

$$I_{\text{add}} = \Gamma_c\left(I_T - A_s r^2\right) + (1 - \Gamma_c)\rho_r A_r {h_r}^2 \tag{20}$$

Eq. (21) results by normalization of the two sides of Eq. (20) and dividing the same by I_T around composite cross-sectional axes

$$\frac{I_{\text{add}}}{I_T} = \Gamma_c\left(1 - \frac{A_s r^2}{I_T}\right) + (1 - \Gamma_c)\frac{\rho_r A_r {h_r}^2}{I_T} = n^2 \tag{21}$$

The effects of materials and geometrical properties of the real composite cross section on the additional flexural stiffness are observed through normalization in Eq. (21). By adding flexural stiffness of the plates added to the equivalence cross section, a function similar to Eq. (22) is achieved

$$I_{\text{add}} = \frac{C_{\text{add}}\, t_{\text{add}}^3}{6} + \frac{2h_{\text{add}}^3\, t_{\text{add}}}{3} + \frac{d^2 h_{\text{add}}\, t_{\text{add}}}{2} + d h_{\text{add}}^2\, t_{\text{add}} \tag{22}$$

By dividing the two sides of Eq. (22)

$$\frac{I_{\text{add}}}{I_T} = \frac{\frac{C_{\text{add}}\, t_{\text{add}}^3}{6} + \frac{2h_{\text{add}}^3\, t_{\text{add}}}{3} + \frac{d^2 h_{\text{add}}\, t_{\text{add}}}{2} + d h_{\text{add}}^2\, t_{\text{add}}}{I_T} \tag{23}$$

By equalizing the two rights sides of Eqs. (21) and (22), another formula is found to calculate the stiffener plates' sizes

$$\frac{\frac{C_{\text{add}}\, t_{\text{add}}^3}{6} + \frac{2h_{\text{add}}^3\, t_{\text{add}}}{3} + \frac{d^2 h_{\text{add}}\, t_{\text{add}}}{2} + d h_{\text{add}}^2\, t_{\text{add}}}{I_T} = n^2 \tag{24}$$

Finite-Element Modeling and Applying Suggested Method

The final purpose of the method suggested in this study is that the PEC cross section is equalized with the fictitious steel cross section. Evidently, this method is merely practical for linear analysis. Therefore, accuracy and reliability of the suggested method will be evaluated by member internal forces by comparing the composite structure analysis results. To ensure the suggested method, in the following *Abaqus 6.14.2* finite-element program two 2-floor and 2-span structures are analyzed under gravity and lateral loads, and the column internal forces (axial, shear, and bending moment loads) of the steel structure are compared with the fictitious steel columns and a structure with PEC columns. Prior to the focus on finite-element analysis, the validation of the PEC numerical model using an experimental specimen is conducted.

Numerical Method

The tested specimens were simulated using *Abaqus 6.14.2* software. All of the details of the specimens, interactions, boundary conditions, and materials were accurately modeled based on the test reports. The steel section of the PEC column is constructed with thin plates, which are susceptible to local buckling causing large rotations at the flange plates, adding geometric nonlinearity to the behavior. In the tests, Column PEC-1 reached ultimate capacity at the simultaneous occurrence of local buckling of the thin flanges and crushing of the concrete. To capture this behavior, S4R shell elements were used to model the steel plates and C3D8R elements were selected to model the weld and concrete blocks between the flange plates and the two webs of the composite section. The transverse links and longitudinal rebars were modeled using B31 beam elements, which is a special beam element using linear interpolation and allowing for transverse shear deformation. The interactions between the concrete and the steel section, including steel flanges and web, were simulated in the model because there was no separation between the concrete and steel section until local buckling occurred in the column flanges. The contact pair algorithm was chosen to model the interactions in the columns. The penalty contact algorithm was finally chosen. The basic Coulomb friction model is used in the penalty contact algorithm, in which the tangential forces in the contacted surfaces are modeled. A concrete damage plasticity (CDP) model in *Abaqus* is used to simulate the behavior of concrete. This model is a continuum plasticity-based damage model that assumes tensile cracking and compressive crushing to be the two main failure mechanisms of the concrete material. The compressional and tensile damage parameters are considered as the linear functions of inelastic strains.

The model proposed by Hsu and Hsu (1994) was used to determine the compressive stress-strain ratio of the concrete. This model may be used for concrete with a maximum compressive strength of 62 MPa, and it calculates compressive stress values from $0.5\sigma_{cu}$ on the ascending part to $0.5\sigma_{cu}$ on the descending part. In this model, compressive stress is found using Eq. (25)

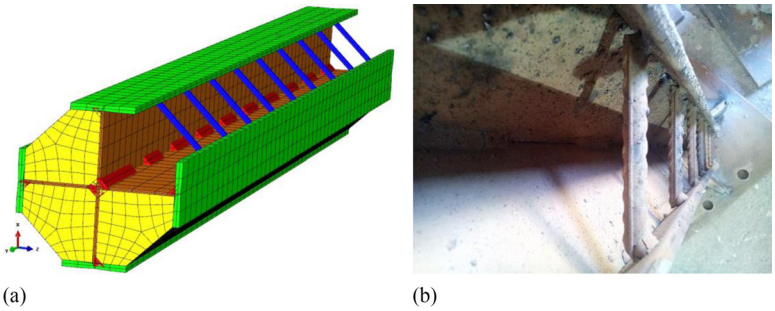

(a) (b)

Fig. 14. (a) Numerical validation model using *Abaqus* and (b) experimental PEC-1 test

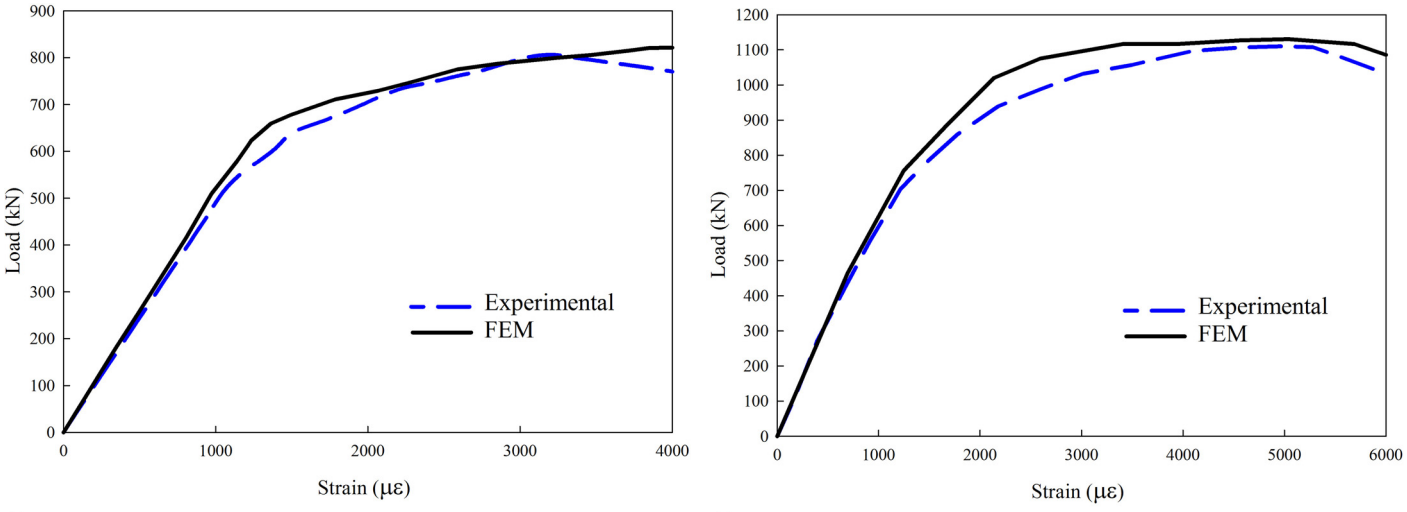

(a) (b)

Fig. 15. Load-displacement curve compared between FEM and the experimental results of (a) Column PEC-1 and (b) Column PEC-2

Pract. Period. Struct. Des. Constr., 2018, 23(3): 04018012

$$\sigma_c = \left(\frac{\beta \left(\frac{\varepsilon_c}{\varepsilon_0} \right)}{\beta - 1 + \left(\frac{\varepsilon_c}{\varepsilon_0} \right)^{\beta}} \right) \sigma_{\text{cu}} \tag{25}$$

$$\beta = \frac{1}{1 - \left[\frac{\sigma_{\text{cu}}}{\varepsilon_0 E_0} \right]}, \ \varepsilon_0 = 8.9 \times 10^{-5} \sigma_{\text{cu}} + 2.114 \times 10^{-3} \tag{26}$$

$$E_0 = 1.2431 \times 10^2 \sigma_{\text{cu}} + 3.28312 \times 10^3 \tag{27}$$

In this study, The mode of Nayal and Rasheed (2006) was used to plot the stress-strain relationship at the tension area. To prevent run-time error, there is a decrease from ultimate stress σ_t to $0.8\sigma_t$ in the *Abaqus* software. Eq. (28) is used to find maximum tensile stress

$$\sigma_t = 0.3(\sigma_c)^{\frac{2}{3}} \tag{28}$$

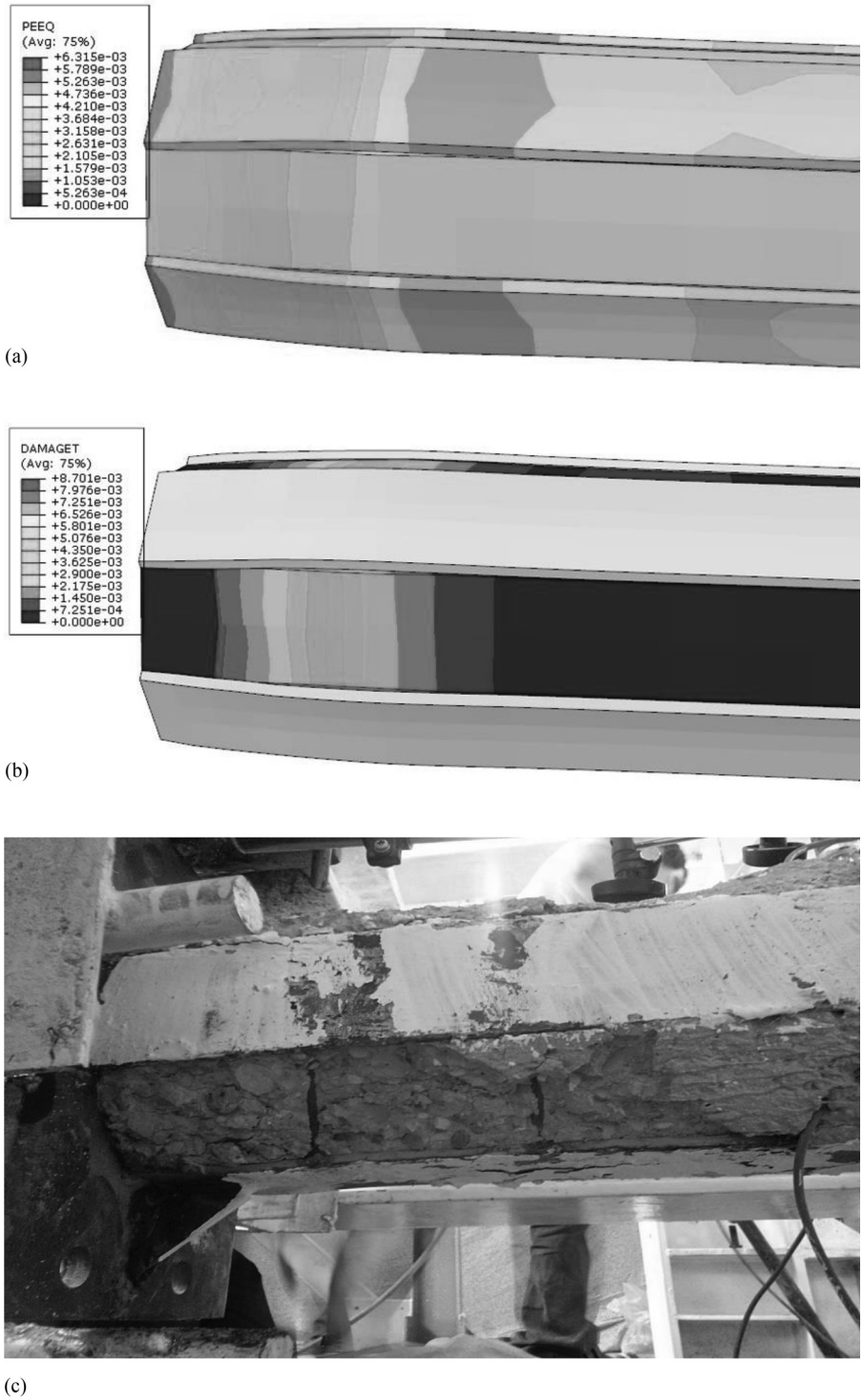

Fig. 16. Buckling faces and concrete crushing at the peak load of Column PEC-1: (a) plastic strain distribution; (b) tensile damage contour in concrete; (c) failure mode of PEC-1 at the peak load

Pract. Period. Struct. Des. Constr., 2018, 23(3): 04018012

The nonlinear behavior of steel and weld elements is simulated using an isotropic hardening model based on the von Mises yield criterion. Both material and structural nonlinearities are considered and solved using the incremental-interactive method in *Abaqus*. The model replicated the experimental PEC-1 and numerical simulation, as shown in Fig. 14.

Comparison of Numerical Simulation with Experimental Results

In this section, to assess the capability of the developed numerical model in simulating the PEC columns, the results of the conducted tests are used to verify and calibrate the developed numerical model in *Abaqus*. In a simulation of the loading condition, a given displacement control in Test PEC-1 is imposed. Figs. 15(a and b) show the comparison of the numerical simulation with the test results. Considering comparing the charts in two linear and nonlinear areas, it shows a good agreement in the initial elastic stiffness and slope of the second part of the curve. It can be concluded that the finite-element model and material constitutive adopted in this paper are reasonable. Fig. 16 indicates the buckling faces and concrete crushing at the peak load in the numerical model and experimental test of PEC-1. Analyses were executed to validate the performance of local buckling under the compressive stress of shell elements used for the steel and the axial capacity of the concrete brick elements used for the concrete. The factors affecting the nonlinear behavior of PEC columns include the width-thickness ratio of steel plates, the area of the longitudinal rebar, and the geometrical parameter of the steel links, such as diameter and interval distance. Using numerical analysis, the effects of those factors on the PEC column capacity and deformability were studied parametrically on the base of the monotonic loading analysis. Four of the most important factors, the interval distance and diameter of links, length of welding line, and the width-thickness ratio of steel plates, are demonstrated.

Parametric Study

In this section, the association between the parameters affecting the compressive behavior of the octagonal PEC column and its compression bearing capacity is sought. Therefore, 30 numerical models were developed regarding Column PEC-2, and parametric studies of those models were conducted. As detailed in previous sections of the paper, laboratory works are time-consuming, expensive, and stressful. To develop the application range of PEC columns made up of normal-strength and high-strength concrete under axial loading, it is necessary to use a parametric model instead of a numerical one.

In this section, the developed numerical model is used to analyze the effects of geometric parameters and materials on PEC columns' behavior. Precision and accuracy of the numerical model mentioned in the previous section compared with laboratory and numerical results were presented. To design the parametric study, the specifications of materials and the geometry of PEC columns were considered as primary variables. In this regard, the cross section of the column (b_f, d), the longitudinal distance between crosslinks (s), and thickness of the flange plate (t_f) as well as web plate thickness (t_w) were regarded as the most significant geometrical parameters. The compressive strength of the concrete in the column is considered as the sole variable of the materials. The geometrical specifications were introduced in a dimensionless value for comparison purposes. Table 8 shows specifications of the numerical models: in the specimen column N and H refer to normal-strength concrete and high-strength concrete.

Table 8. Characteristics of the Columns

E_c (MPa)	ε_{cu} ($\mu\varepsilon$)	f_{cu} (MPa)	s/d	b/t	Specimen
23,500	1,900	25	0.33	5	PEC-N1
23,500	1,900	25	0.67	5	PEC-N2
23,500	1,900	25	1.00	5	PEC-N3
23,500	1,900	25	0.33	10	PEC-N4
23,500	1,900	25	0.67	10	PEC-N5
23,500	1,900	25	1.00	10	PEC-N6
23,500	1,900	25	0.33	20	PEC-N7
23,500	1,900	25	0.67	20	PEC-N8
23,500	1,900	25	1.00	20	PEC-N9
23,500	1,900	25	0.33	30	PEC-N10
23,500	1,900	25	0.67	30	PEC-N11
23,500	1,900	25	1.00	30	PEC-N12
23,500	1,900	25	0.33	35	PEC-N13
23,500	1,900	25	0.67	35	PEC-N14
23,500	1,900	25	1.00	35	PEC-N15
36,400	2,500	60	0.33	5	PEC-H1
36,400	2,500	60	0.67	5	PEC-H2
36,400	2,500	60	1.00	5	PEC-H3
36,400	2,500	60	0.33	10	PEC-H4
36,400	2,500	60	0.67	10	PEC-H5
36,400	2,500	60	1.00	10	PEC-H6
36,400	2,500	60	0.33	20	PEC-H7
36,400	2,500	60	0.67	20	PEC-H8
36,400	2,500	60	1.00	20	PEC-H9
36,400	2,500	60	0.33	30	PEC-H10
36,400	2,500	60	0.67	30	PEC-H11
36,400	2,500	60	1.00	30	PEC-H12
36,400	2,500	60	0.33	35	PEC-H13
36,400	2,500	60	0.67	35	PEC-H14
36,400	2,500	60	1.00	35	PEC-H15

This section addresses the effect of each parameter on the behavior of the octagonal composite columns suggested in this paper. The output parameters of the parametric study are axial force (P_u) and mean axial strain ($\varepsilon_{a,u}$) at failure. Mean axial strain was determined by averaging total displacement in the longitudinal direction divided by the length of the column. In most of the cases, a local buckling in the section was observed between the two links. Significant observations during the parametric studies were reported, and force-displacement curves were developed. The sample PEC-N5 column is the same as the PEC-2 sample of the validated laboratory model.

Effect of Width-Thickness Ratio of Flange on Compressive Capacity

Table 9 shows the effect of the flange slenderness ratio of the column's steel section on the compression bearing capacity. In the table, n_p represents the percentage of difference between the compressive force of each sample and the reference sample of the group, whereas n_ε represents the percentage of difference between the axial strain of each sample and the reference sample. As the results suggest, in each group of samples there is an increase of flange slenderness ratio (width-thickness ratio), and the compression bearing capacity of the column decreases significantly (at most 42%). In the case of the corresponding axial strain with maximum force, it should be noted that the slenderness ratio parameter of the flange

Table 9. Effect of Flange Slenderness on Compressive Capacity and Axial Strain

n_ε (%)	n_p (%)	Axial strain ($\mu\varepsilon$)	P_u (kN)	f_{cu} (MPa)	s/d	b/t	Specimen	Group
0	0	3,126	1,307.4	25	0.33	5	PEC-N1[a]	1
−2	−7	3,048	1,213.1	25	0.33	10	PEC-N4	
−3	−14	3,020	1,125.6	25	0.33	20	PEC-N7	
−4	−27	2,995	952.4	25	0.33	30	PEC-N10	
−5	−35	2,984	856.2	25	0.33	35	PEC-N13	
0	0	3,104	1,252.6	25	0.67	5	PEC-N2[a]	2
−1	−12	3,058	1,105.4	25	0.67	10	PEC-N5	
−3	−13	3,022	1,090	25	0.67	20	PEC-N8	
−4	−25	2,994	946.7	25	0.67	30	PEC-N11	
−4	−34	2,989	834.1	25	0.67	35	PEC-N14	
0	0	2,965	1,237.2	25	1.00	5	PEC-N3[a]	3
+3	−8	3,057	1,141.9	25	1.00	10	PEC-N6	
+2	−12	3,019	1,094.8	25	1.00	20	PEC-N9	
+1	−23	2,990	945.7	25	1.00	30	PEC-N12	
0	−33	2,973	820.6	25	1.00	35	PEC-N15	
0	0	3,741.2	1,791.1	60	0.33	5	PEC-H1[a]	4
−1	−4	3,687.6	1,722.6	60	0.33	10	PEC-H4	
−2	−5	3,674	1,698.8	60	0.33	20	PEC-H7	
−3	−11	3,634	1,597.4	60	0.33	30	PEC-H10	
−3	−20	3,610.8	1,426	60	0.33	35	PEC-H13	
0	0	3,734.8	1,784.4	60	0.67	5	PEC-H2[a]	5
−1	−9	3,679.6	1,629.4	60	0.67	10	PEC-H5	
−2	−14	3,666.4	1,628.3	60	0.67	20	PEC-H8	
−4	−12	3,592.8	1,576.3	60	0.67	30	PEC-H11	
−4	−27	3,596.8	1,299.5	60	0.67	35	PEC-H14	
0	0	3,658	1,731.8	60	1.00	5	PEC-H3[a]	6
+1	−7	3,678.4	1,623.6	60	1.00	10	PEC-H6	
0	−7	3,672.8	1,617.2	60	1.00	20	PEC-H9	
−2	−12	3,598	1,529.3	60	1.00	30	PEC-H12	
−2	−27	3,597.6	1,271.4	60	1.00	35	PEC-H15	

[a]Reference specimen in specific group.

Note: Negative sign represents a value less than the value corresponding to the reference specimen, and the positive sign indicates a value bigger than the reference specimen.

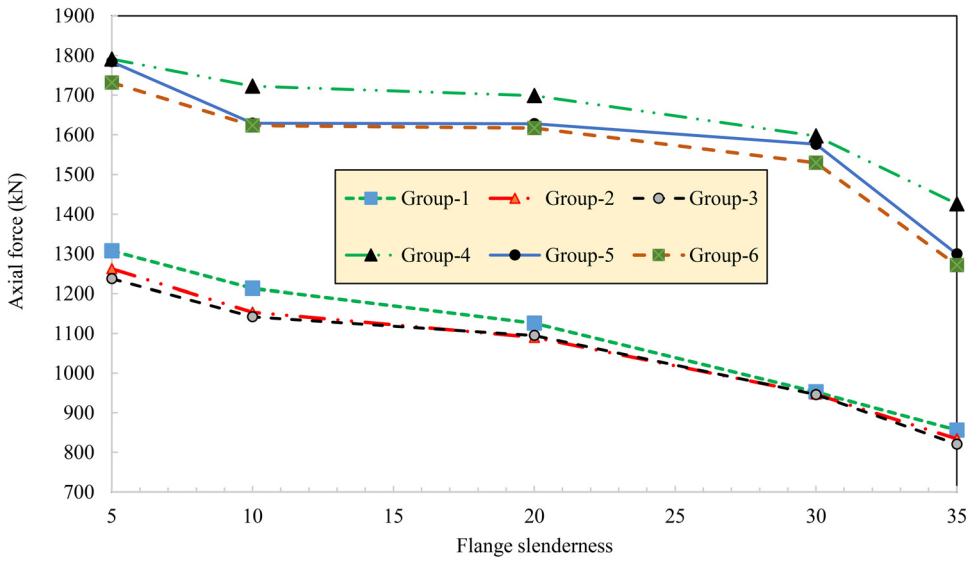

Fig. 17. Effect of flange slenderness on load-bearing capacity

does not significantly affect its variation trend. Fig. 17 shows the variation of the compression bearing capacity in relation to the slenderness ratio of the flange. As shown in Fig. 17, the change and increase of the slenderness ratio of the flange are followed by more a significant decline slope of the bearing capacity, especially if the ratio increases from 30 to 35. This is the ultimate and allowable

Pract. Period. Struct. Des. Constr., 2018, 23(3): 04018012

range (slenderness ratio 32) that the CSA S16-14 standard recommends.

In the case of an increase of b_f/t ratio from 30 to 35, the bearing capacity of all six groups of PEC columns reduces in a range from 11 to 35% (for different link distances, of course). The mean decline of the bearing capacity of samples with normal-strength concrete is almost 15%, whereas for the samples with high-strength concrete, the mean decline is almost 11%.

Effect of Link Distance to Section Depth Ratio on Compressive Capacity

Table 10 presents the effect of the parameter of ratio of the transverse link distance (s) to the depth of section (d) on the variation of bearing capacity. Despite variation of the s/d ratio and the increase of variation of the flange slenderness ratio (b_f/t), the bearing capacity did not vary significantly (at most 9%). The maximal decline of the bearing capacity of the high-strength concrete sample PEC-H14 was 9%. The comparison of different force-strain curves (Fig. 18) of specimens with different s/d ratios suggests that a decrease of the ratio is followed by little improvement of ductility (here ductility is getting more stretches as area below the curve increases; the qualitative aspect is taken into account). Although different ranges of the s/d ratio did not significantly affect the axial bearing capacity of the column, force-axial strain curves for small s/d ratios are more adjustable. However, this effect is more significant in the case of columns with thinner flanges.

Effect of Compressive Strength of Concrete on Compressive Capacity

The effect of the compressive strength of normal-strength concrete (25 MPa) and high-strength concrete (60 MPa) on the compressive bearing capacity of the column is shown in Fig. 19. The axial bearing capacity of the columns made up of high-strength concrete increased on average 51% compared with normal-strength concrete. The response of the axial force–axial strain of PEC columns made up of high-strength concrete signifies a higher slope of specimens in the initial part of the curves. This is because the elasticity modulus of high-strength concrete is almost 38% more than that of normal-strength concrete. In addition, the columns made of high-strength concrete suggest that strength after peak load drops at a higher slope compared with columns made up of normal-strength concrete. In addition, the ductility of columns reduces when using high-strength concretes.

Assessment of Equalized Section Approach

The plan and perspective of a building with irregular geometry are shown in Fig. 20. This paper is focused on the behavior of a

Table 10. Effect of Link Spacing on Compressive Capacity and Axial Strain

n_ε (%)	n_p (%)	Axial strain ($\mu\varepsilon$)	P_u (kN)	f_{cu} (MPa)	s/d	b/t	Specimen
0	0	3,126	1,307.4	25	0.33	5	PEC-N1[a]
−1	−3	3,104	1,262.2	25	0.67	5	PEC-N2
−5	−6	2,965	1,237.2	25	1.00	5	PEC-N3
0	0	3,048	1,213.1	25	0.33	10	PEC-N4[a]
0	−8	3,058	1,105.4	25	0.67	10	PEC-N5
0	−6	3,057	1,141.9	25	1.00	10	PEC-N6
0	0	3,020	1,125.6	25	0.33	20	PEC-N7[a]
0	−5	3,022	1,070.8	25	0.67	20	PEC-N8
0	−5	3,019	1,065.9	25	1.00	20	PEC-N9
0	0	2,995	952.4	25	0.33	30	PEC-N10[a]
0	−1	2,994	946.7	25	0.67	30	PEC-N11
0	−1	2,990	945.7	25	1.00	30	PEC-N12
0	0	2,984	856.2	25	0.33	35	PEC-N13[a]
0	−3	2,989	834.1	25	0.67	35	PEC-N14
0	−4	2,973	820.6	25	1.00	35	PEC-N15
0	0	3,741.2	1,791.1	60	0.33	5	PEC-H1[a]
0	0	3,734.8	1,784.4	60	0.67	5	PEC-H2
−2	−3	3,658	1,731.8	60	1.00	5	PEC-H3
0	0	3,687.6	1,722.6	60	0.33	10	PEC-H4[a]
0	−5	3,679.6	1,629.4	60	0.67	10	PEC-H5
0	−6	3,678.4	1,623.6	60	1.00	10	PEC-H6
0	0	3,674	1,698.8	60	0.33	20	PEC-H7[a]
0	−4	3,666.4	1,628.3	60	0.67	20	PEC-H8
0	−5	3,672.8	1,617.2	60	1.00	20	PEC-H9
0	0	3,634	1,597.4	60	0.33	30	PEC-H10[a]
−1	−2	3,592.8	1,576.3	60	0.67	30	PEC-H11
−1	−5	3,598	1,529.3	60	1.00	30	PEC-H12
0	0	3,610.8	1,426	60	0.33	35	PEC-H13[a]
0	−8	3,596.8	1,299.5	60	0.67	35	PEC-H14
0	−9	3,597.6	1,271.4	60	1.00	35	PEC-H15

[a]Reference specimen in specific group.

Note: Negative sign represents a value less than the value corresponding to the reference specimen, and the positive sign indicates a value bigger than the reference specimen.

Pract. Period. Struct. Des. Constr., 2018, 23(3): 04018012

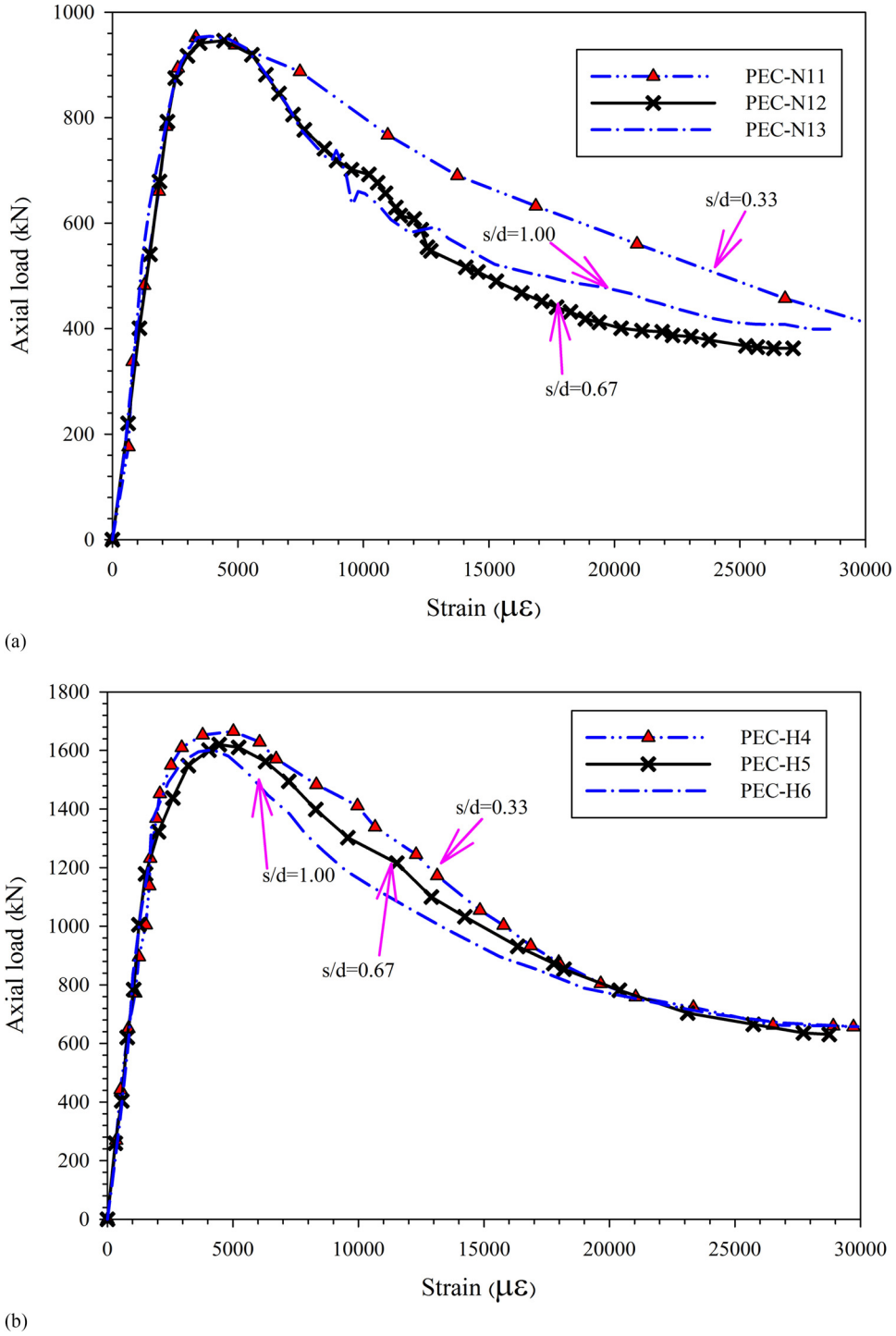

Fig. 18. Effect of *s/d* on the axial load–axial strain relationship of specimens with (a) normal-strength concrete and (b) high-strength concrete

geometrically irregular building with a combination of steel beam and PEC columns, which has not been studied before. The column sizes in both structures are listed in Table 11. In both structures a similar H-shaped beam is used (flange width 150 mm, depth 250 mm, and flange and web thickness 10 and 8 mm, respectively). The height of each floor is equal to 4 m. The purpose is to find the internal forces of the column member in the structures. To decrease analysis time concrete slab modeling is ignored and the dead load is directly imposed to the beams.

Two analyses were conducted on the structures. In the first analysis, only a dead load equal to 6 kN/m^2 was imposed on the surface of the ceiling of the assumed slab. Under such a state, the load was applied manually onto the beams compressing the flange. In the second analysis, in addition to keeping the gravity load constant within the analysis, the lateral load equal to 300 kN was applied to the center of the roof ceiling surface by exercising the reference point. After the analysis, the axial and shear forces and bending moment in Tables 12 and 13 were found for the B-2 and C-2 columns on the first floor. Tables 12 and 13 list the value difference between the column internal forces in the two studied structures as around 1%, which in turn enables the practicality of the suggested method in PEC columns equalization.

Pract. Period. Struct. Des. Constr., 2018, 23(3): 04018012

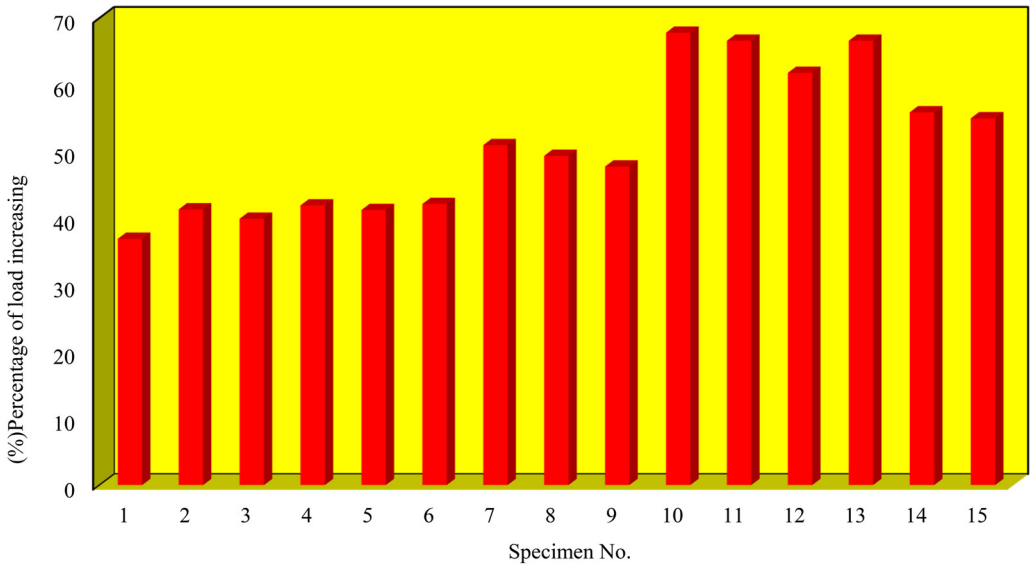

Fig. 19. Effect of concrete strength on the compressive capacity of specimens

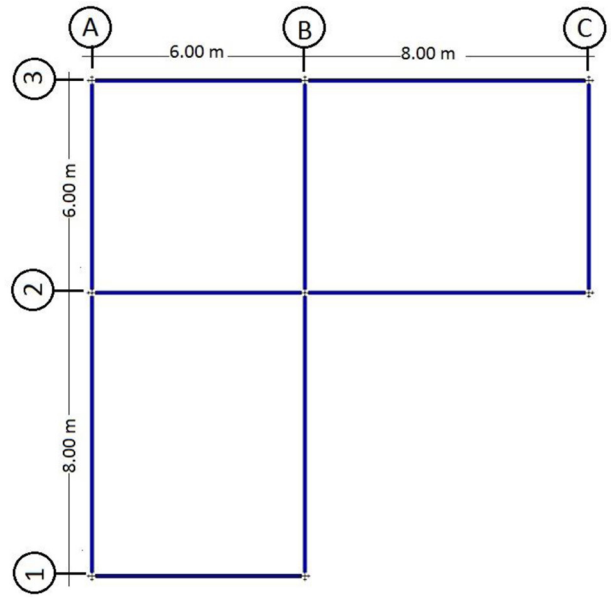

(a)

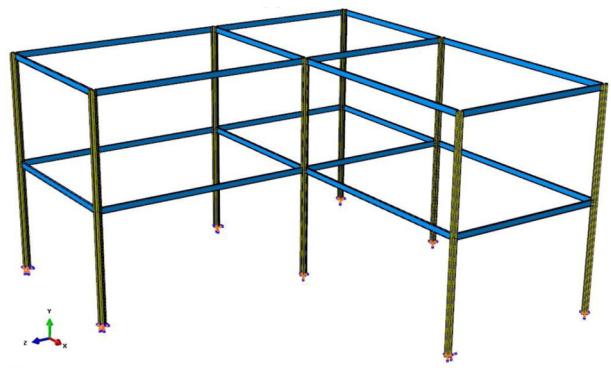

(b)

Fig. 20. (a) Plan view of an irregular building and (b) perspective view of a building with boundary conditions (Units: meters)

Table 11. Dimensions of Equivalent Steel Section for PEC Column

Frame	Section characteristic	Dimension (mm)
Composite frame	d	300
	b_f	150
	t_f	6
	t_w	3
	h_r	75
	ϕ	14
Bare steel frame	b_e	247
	C_{add}	125
	h_{add}	125
	t_{add}	6

Concluding Remarks

In this article, two PEC columns were tested under monotonic compressive loading. To make practical utilization of such cross sections in structural design programs, such as *SAP 19.0.0*, the equalization method of these cross sections using fictitious steel cross sections was presented and studied. In this method the technique to equalize the compressing strength and the flexural stiffness of the two cross sections was applied. Also, at the end an example of a geometrically irregular structure using two types of steel and PEC columns was presented under gravity and lateral loading. The most significant findings of this research are given in the following:

1. Adding longitudinal bars results in an increase in load-bearing capacity for roughly 20%, and the interaction between concrete and the steel plate wall also increases load-bearing capacity by approximately 5%.
2. The average predicted-to-test capacity ratio of the PEC columns made with normal-strength concrete (without reinforcement) was 1.14. For the concrete reinforcement with rebars, the average ratio was 1.02. By comparing the test results of this study with the CSA S16-14 equation, it was found that this equation is conservative for use with PEC columns. These design calculations reduce the capacity of the steel flanges to

Table 12. Comparison of Internal Forces under Vertical Loads Only

Column ID	$M_{x,\text{steel}}$	$M_{x,\text{comp}}$	$M_{z,\text{steel}}$	$M_{z,\text{comp}}$	$N_{y,\text{steel}}$	$N_{y,\text{comp}}$	$V_{y,\text{steel}}$	$V_{y,\text{comp}}$	$V_{z,\text{steel}}$	$V_{z,\text{comp}}$
B-2	13.44	13.37	0	0	399.14	398.64	0	0	6.07	6.11
C-2	4.87	4.88	0	0	144.73	144.97	0	0	2.44	2.42

Note: Forces in kilonewtons and moments in kilonewton meters.

Table 13. Comparison of Internal Forces under Vertical Loads and Horizontal Loads of 300 kN

Column ID	$M_{x,\text{steel}}$	$M_{x,\text{comp}}$	$M_{z,\text{steel}}$	$M_{z,\text{comp}}$	$N_{y,\text{steel}}$	$N_{y,\text{comp}}$	$V_{y,\text{steel}}$	$V_{y,\text{comp}}$	$V_{z,\text{steel}}$	$V_{z,\text{comp}}$
B-2	367.44	366.42	633.18	633.65	448.35	448.02	200.31	199.66	211.36	210.98
C-2	243.67	244.08	192.58	192.88	162.72	161.33	112.36	113.44	115.44	114.77

Note: Forces in kilonewtons and moments in kilonewton meters.

account for their susceptibly to local buckling between the links. However, flange buckling was not observed before the peak load.

3. The suggested method managed to give results close to those of the composite specimen in terms of compressing strength and flexural stiffness as well as internal forces of the members.
4. The accuracy of the suggested method was studied by analyzing two structures with fictitious steel columns and PEC columns. In this comparison, the axial, shearing forces, and bending moment were compared. The capability of this method for linear static analysis was demonstrated. Therefore, the suggested method may be applied in all structural designing tasks by the engineers because it has met the needs of the designers to benefit from time-consuming and difficult finite-element programs as well as the need for professional and skilled users.

References

Abaqus v 6.14.2 [Computer software]. SIMULIA, Providence, RI.

ACI (American Concrete Institute). (1997). "State-of-the-art report on high-strength concrete (reapproved in 1997)." *ACI 363R-92*, Farmington Hills, MI.

ACI (American Concrete Institute). (2008). "Building code requirements for structural concrete and commentary." *ACI 318R-08*, Farmington Hills, MI.

ANSYS 18.2 [Computer software]. ANSYS, Canonsburg, PA.

ASTM. (2003). "*Standard test methods and definitions for mechanical testing of steel products*," West Conshohocken, PA.

Begum, M., Driver, R., and Elwi, A. (2007). "Finite-element modeling of partially encased composite columns using the dynamic explicit method." *J. Struct. Eng.*, 10.1061/(ASCE)0733-9445(2007)133:3(326), 326–334.

Begum, M., Driver, R. G., and Elwi, A. E. (2013). "Behaviour of partially encased composite columns with high strength concrete." *Eng. Struct.*, 56(Nov), 1718–1727.

Begum, M., Driver, R. G., and Elwi, A. E. (2015). "Parametric study on eccentrically-loaded partially encased composite columns under major axis bending." *Steel Compos. Struct.*, 19(5), 1299–1319.

Begum, M., and Ghosh, D. (2014). "Simulations of PEC columns with equivalent steel section under gravity loading." *Steel Compos. Struct.*, 16(3), 305–323.

CEN (European Committee for Standardization). (2004). *Eurocode 4: Design of composite steel and concrete structures, part 1-1: General rules and rules for buildings*, Brussels, Belgium.

Chen, Y., Wang, T., Yang, J., and Zhao, X. (2010). "Test and numerical simulation of partially encased composite columns subject to axial and cyclic horizontal loads." *Int. J. Steel Struct.*, 10(4), 385–393.

Chicoine, T., Massicotte, B., and Tremblay, R. (2002a). "Finite element modelling and design of partially encased composite columns." *Steel Compos. Struct.*, 2(3), 171–194.

Chicoine, T., Tremblay, R., Massicotte, B., Ricles, J., and Lu, L. (2002b). "Behavior and strength of partially encased composite columns with built up shapes." *J. Struct. Eng.*, 10.1061/(ASCE)0733-9445(2002)128:3(279), 279–288.

CSA (Canadian Standards Association). (2014). "Limit states design of steel structures." *S16–14*, Mississauga, ON, Canada.

Dastfan, M., and Driver, R. (2016). "Large-scale test of a modular steel plate shear wall with partially encased composite columns." *J. Struct. Eng.*, 10.1061/(ASCE)ST.1943-541X.0001424, 04015142.

Ebadi Jamkhaneh, M., and Kafi, M. A. (2017). "Experimental and numerical investigation of octagonal partially encased composite columns subject to axial and torsion moment loading." *Civil Eng. J.*, 3(10), 939–955.

Hsu, L. S., and Hsu, C. T. T. (1994). "Complete stress-strain behaviour of high-strength concrete under compression." *Mag. Concr. Res.*, 46(169), 301–312.

Marinopoulou, A. A., Balopoulos, V. D., and Kalfas, C. N. (2007). "Simulation of partially encased composite steel–concrete columns with steel columns." *J. Constr. Steel Res.*, 63(8), 1058–1065.

Nayal, R., and Rasheed, H. (2006). "Tension stiffening model for concrete beams reinforced with steel and FRP bars." *J. Mater. Civ. Eng.*, 10.1061/(ASCE)0899-1561(2006)18:6(831), 831–841.

Oyawa, W. O., Gathimba, N. K., and Mang'uriu, G. N. (2016). "Structural response of composite concrete filled plastic tubes in compression." *Steel Compos. Struct.*, 21(3), 589–604.

Pereira, F. M., De Nardin, S., and El Debs, L. H. C. (2016). "Structural behavior of partially encased composite columns under axial loads." *Steel Compos. Struct.*, 20(6), 1305–1322.

SAP 19.0.0 [Computer software]. Computers & Structures, Inc., Walnut Creek, CA.

Song, Y. C., Wang, R. P., and Li, J. (2016). "Local and post-local buckling behavior of welded steel shapes in partially encased composite columns." *Thin Walled Struct.*, 108(Nov), 93–108.

Zhao, G. T., and Feng, C. (2012). "Axial ultimate capacity of partially encased composite columns." *Appl Mech. Mater.*, 166–169, 292–295.